Effects of Collisional-Radiative Processes with Relative Drift in Electric Propulsion Devices

IEPC-2019-A191

Presented at the 36th International Electric Propulsion Conference
University of Vienna, Austria
September 15-20, 2019

Richard J. E. Abrantes*
National Research Council Research Associateship, Washington, D.C., 20001, USA

Robert Lilly†
ERC Inc., Edwards AFB, California, 93524, USA

Robert Martin‡
Air Force Research Laboratory, Edwards AFB, California, 93524, USA

Abstract: As future spacecraft missions begin to demand higher performance characteristics from its electric propulsion systems, the complexity of new thruster systems and operations will increase to meet these objectives. However, the arrival of these new potential thrusters will involve greater challenges to overcome such as new plasma physics phenomena under the context of electric propulsion. In this work, the Field-Reversed-Configuration thruster is presented as one such device with strong multifluid effects that are necessarily part of the thruster's operation. These multifluid effects are important not only for the ionization of the plasma, but for the formation of the plasmoid that will lead to thrust. Therefore, the reaction kinetics involving multifluid effects will be the focus of discussion and analysis in this study to convey its significance for such thrusters. Steady-state and time-dependent simulations incorporating the multifluid rate coefficients were performed showing the multifluid effect's impact on the plasma parameters relevant to new, forthcoming propulsion devices.

I. Introduction

As the complexity of new electric propulsion (EP) systems increases, there is a growing need to understand the multiphysics and multiscale nature of the plasma dynamics within these devices. One such device that exemplifies the increasing complexity of these forthcoming propulsion devices is the Field-Reversed Configuration (FRC) thruster.[1,2] The FRC thruster is an EP device that employs a two-step process to generate thrust. Each thrust cycle begins with the formation of the plasmoid through the induced magnetic field generated by the azimuthally-driven electron stream. This plasmoid is formed once the induced magnetic field encloses upon itself, hence "Field-Reversed Configuration", after which a set of external coils are modulated to eject the plasmoid out of the thruster channel. In comparison with current EP technology, this device presents greater challenges as this electromagnetic device operates through highly-transient conditions, requiring thorough plasma ionization, plasmoid formation configured through the magnetic field's reversal, and proper modulation of the coils for plasmoid ejection.[3]

Since the operation of the FRC thruster is highly dependent on the efficacy of plasmoid ejection, the formation of the plasmoid is an important, foundational phase that must be realized for each thrust cycle. The intricacies of FRC formation requires resolving as many physical processes as possible that contribute towards

*NRC Postdoctoral Research Associate, AFRL/RQRS (In-Space Propulsion Branch), richard_june.abrantes.ctr@us.af.mil
†Research Engineer, AFRL/RQRS (In-Space Propulsion Branch), robert.lilly.3.ctr@us.af.mil
‡Computational Scientist, AFRL/RQRS (In-Space Propulsion Branch), robert.martin.101@us.af.mil

each plasmoid ejection sequence. Recently, multifluid codes have been developed simply to investigate the influence of electromagnetic fields on the plasmoid formation process.[4] The goal of these initial simulations is to study the likelihood of plasmoid formation due to the interactions between the plasma fluids and the electromagnetic field. But, the study of electromagnetic coupling within FRC plasmoids is only one important facet of the entire formation sequence; a more realistic simulation of the plasmoid's formation requires coupling the plasma reaction kinetics within this multifluid environment.

In this work, a collisional-radiative model was employed to capture the reaction kinetics within an FRC simulation. The collisional-radiative model monitors the variations in the atomic state distribution (ASD) as well as other impacted properties like temperature due to the collisional and radiative processes occurring within the plasma system. The rate coefficients that are calculated and used in collisional-radiative models conventionally assume non-streaming heavy species (atomic) and electron energy distributions. By contrast, the FRC operation is characterized by a strong toroidal electron current flow moving perpendicular to the axially streaming ions. Therefore, any CR model that is coupled to an FRC simulation, or any device with strong multifluid characteristics, should account for relative streaming corrections in the collisional rate calculations. Rate coefficients modified for relative streaming effects will be incorporated into the CR model to show the impact of the multifluid phenomena on the reaction kinetics.[5,6] These modified reaction kinetics are crucial as the inelastic processes couple to the multifluid FRC formation.

This paper is organized as follows: Section II will discuss the appropriate modifications to the rates as derived from a previous work, after which rate maps and steady-state simulation results using the modified rates will be discussed. The calculated rates will also be utilized in Section III where computational results of a time-dependent simulation will be analyzed. This section will briefly address the parameters used for the prototypical, in-house FRC thruster as well as their scalability. This work will then be concluded in Section IV.

II. Atomic Data and Modification of the Rate Equations

In a multiphysics plasma simulation, the collisional-radiative model captures the changes in the atomic state distribution due to the inelastic processes occurring in the plasma. The inelastic processes modeled in this work include electron-impact excitation and deexcitation, electron-impact ionization and its inverse three-body recombination, along with the radiative processes of radiative recombination and spontaneous emission. These processes enter the CR model in the form of rates dictating how quickly each transition occurs from one atomic state to another. However, a sufficiently complete set of atomic and transition data is necessary to generate the rates that are needed in a CR simulation. For this study, cFAC, the C++ variant of the Flexible Atomic Code (FAC), was employed to generate all of the necessary atomic and transition data for the CR calculations.[7] While there is the well-known caveat that these atomic codes based on perturbative methods are inaccurate for near-neutral/low-Z applications, this code is much more complete in its ability to generate data for many different types of transitions. Therefore, the self-consistency associated with generating copious transition data amongst the computed atomic states makes cFAC a viable candidate to study since the entire set of reaction kinetics is coherently modified due to multifluid effects. Although this particular atomic code was used in this study, one should note that this CR model is capable of accommodating more accurate data sets should they become available.

As mentioned, cFAC was used to produce atomic and transition data for this study. While the FRC thruster is capable of utilizing a variety of propellant species, xenon was the element chosen in this work due to its prevalence in many electric propulsion systems. 53 levels of Xe^{+0}, 117 levels of Xe^{+1}, and only 5 levels of Xe^{+2} were included in the simulation to display the code's multistage ionization capabilities. The number of levels chosen for each ion stage was based on the continuum threshold from NIST along with the decision to limit the computational expenses associated with generating the rate coefficient maps.[8] These levels produced a total of 8166 electron-impact excitation channels, 4150 electron-impact ionization channels, and 4150 radiative recombination channels, each bearing cross-sectional data to be integrated within the CR model's rate calculation routine. Lastly, 2600 spontaneous emission transitions generated Einstein A rate coefficients to be used in the model, which obviously do not require any modification for the multifluid effect. The multifluid rate equations used to generate the rate coefficient maps are described in the following subsections.

A. Electron-Impact Excitation and Deexcitation

The first set of processes which will be discussed is electron-impact excitation and deexcitation. The corresponding multifluid rates were derived by Le and Cambier and are shown in Eqs. (2) and (3).[5] These rates were derived by accounting for the properties of both fluids, e.g. temperature and fluid velocity, and performing the integrations over the non-dimensionalized energy space, x, under a center-of-mass (COM) frame. As a result, the excitation and deexcitation rates are augmented by the exponential and $\zeta^{(0)}$ factors that account for the non-dimensionalized multifluid drift energy, λ. The $\zeta^{(0)}$ factor takes the form below:

$$\zeta^{(0)} = \frac{1}{2}\int_{-1}^{+1} dy e^{2\xi y} = \frac{\sinh(2\xi)}{2\xi} \qquad \text{s.t.} \qquad \lim_{\xi \to 0} \zeta^{(0)} = 1 \tag{1}$$

In addition, the deexcitation rate coefficient may be rewritten in terms of the forward excitation cross section by enforcing detailed balance through the Klein-Rosseland relation. Note as well for both equations that the equations converge to the well-known rate coefficient equations when the multifluid effect embodied in λ approaches 0.

$$\Gamma_{sl}^{ex} = N_s N_l \overline{g}_{\tilde{T}} e^{-\lambda} \int_{x=x^*}^{\infty} dx\ x e^{-x} \overline{\sigma}_{sl}^{ex}(x) \zeta^{(0)} \left(\sqrt{\lambda x}\right) \tag{2}$$

$$\Gamma_{su}^{de} = N_s N_u \overline{g}_{\tilde{T}} e^{-\lambda} e^{x^*} \frac{g_l}{g_u} \int_{x=x^*}^{\infty} dx\ x e^{-x} \overline{\sigma}_{sl}^{ex}(x) \zeta^{(0)} \left(\sqrt{\lambda (x - x^*)}\right) \tag{3}$$

Using the cross-sections generated from cFAC and implementing the multifluid rate calculations, 2-dimensional rate coefficient maps as a function of temperature, $\tilde{T}$ (which has been approximated as the electron temperature, T_e), and the COM non-dimensional kinetic energy, λ, were generated for each transition. Two sample sets of transition rate maps are shown below in Figs. 1 and 2.

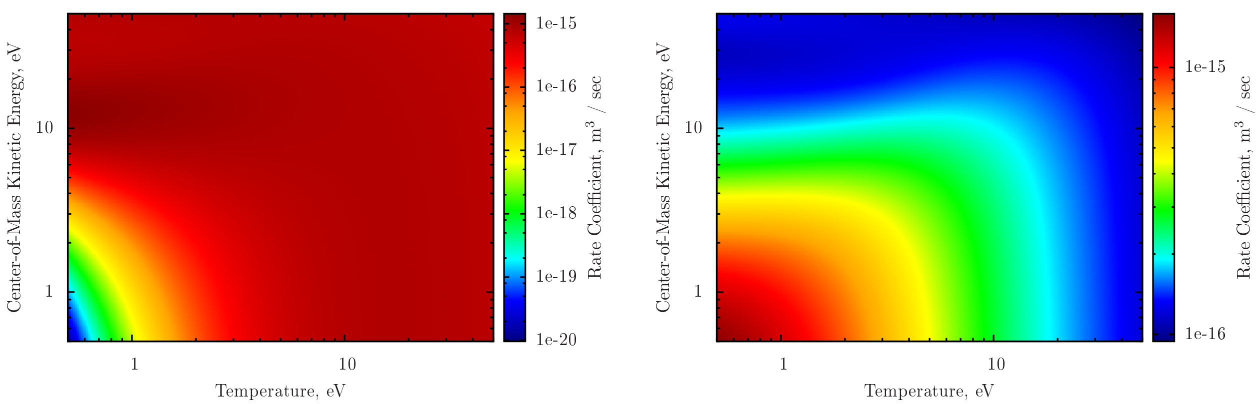

(a) Excitation

(b) Deexcitation

Figure 1: Electron-impact excitation and deexcitation multifluid rate coefficients between (lower state) Xe^{+0} $5p^4_{3/2}(J=0)$ and (upper state) Xe^{+0} $[5p^3_{3/2}(J=0)\ 5d^1_{5/2}(J=5/2)]\ (J=3)$. The energy gap between both states as calculated by cFAC is 9.723 eV.

Figs. 1a and 1b represent the general set of excitation and deexcitation rate coefficient maps that have been tabulated, i.e. most of the rate coefficient maps follow the contour maps shown in these subfigures. As the input parameters approach the abscissa on these maps, the rates are more closely represented by an integration over the thermal distribution, while rates that are much closer to the ordinate correlate to the beam-like rates. In contrast, Figs. 2a and 2b represent the set of excitation and deexcitation rate coefficients for a transition that is spin-forbidden. The allowed transition in 1a requires a threshold energy for the reaction to proceed, hence the eventual rise and peak of the rate coefficient especially closer to the ordinate. However, the strong monotonic dropoff in the forbidden transition's cross-section leads to a profile that is very similar to the deexcitation rate.

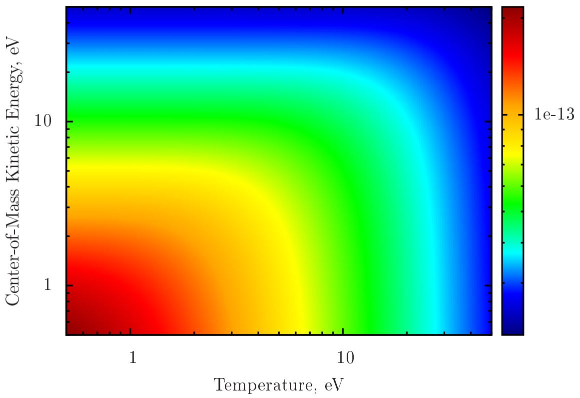

(a) Excitation

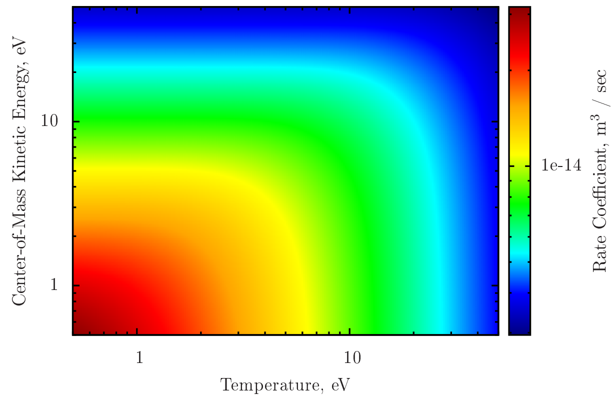

(b) Deexcitation

Figure 2: Electron-impact excitation and deexcitation multifluid rate coefficients between (lower state) Xe^{+0} $[5p^3_{3/2}(J=3/2)\ 6d^1_{3/2}(J=3/2)]\ (J=0)$ and (upper state) Xe^{+0} $[5p^3_{3/2}(J=3/2)\ 6d^1_{3/2}(J=3/2)]\ (J=3)$. The energy gap between both states as calculated by cFAC is 0.0226 eV. Note that these rate coefficient maps are for a spin-forbidden transition.

B. Electron-Impact Ionization and Three-Body Recombination

The next set of inelastic processes to discuss are electron-impact ionization and its inverse three-body recombination process. The rates in Eqs. 4 and 5 were derived in a separate paper by Le and Cambier, but present a heightened challenge due to the third body (electron) entering the inverse collision process.[6] This leads to a familiar formulation in the multifluid ionization rate compared to the two-body processes of excitation and deexcitation, but a more complicated and numerically expensive formula for the three-body recombination process. As one can see, the recombination formula still employs the same exponential and $\zeta^{(0)}$ factors, albeit with an extra $\zeta^{(0)}$ factor due to the introduction of a third body in the process and the use of a differential cross section (DCS) in the integrated cross section's (ICS) stead. Unlike the previous rates, three-body recombination rate coefficient requires the DCS because of the variability in the two electrons' energy difference; this is akin to the incorporation of three-body recombination events in a Vlasov inelastic collision term.

$$\Gamma^{ion}_{sl} = N_s N_l \overline{g}_{\tilde{T}} e^{-\lambda} \int_{x=x^*}^{\infty} dx_0\ x_0 e^{-x_0} \overline{\sigma}^{ion}_{sl}(x_0) \zeta^{(0)} \left(\sqrt{\lambda x_0}\right) \tag{4}$$

$$\Gamma^{rec}_{su} = \frac{g_n}{2 g_i \mathbb{Z}_e} N_u N_s^2 \overline{g}_{\tilde{T}} e^{-2\lambda} e^{x^*} \int_{x^*}^{\infty} dx_0\ x_0\ e^{-x_0} \int_{x^*}^{x_0} \zeta^{(0)} \left(\sqrt{\lambda x_1}\right) \zeta^{(0)} \left(\sqrt{\lambda x_2}\right) \left(\frac{d\sigma^{ion}}{d\nu}\right)\ d\nu \tag{5}$$

Figures 3a and 3b represent the typical rate coefficient maps produced by integrating Eqs. 4 and 5, respectively. Note that the three-body recombination rate uses the ionization cross section in its integration by enforcing detailed balance through the Fowler relation. The map contours are very similar to the "allowed" excitation and deexcitation maps shown previously, where there is a heightened transition likelihood if much of the electron energy lies past beyond the ionization threshold. Likewise with deexcitation, the three-body recombination map decreases as the temperature or COM kinetic energy increases since there is a higher likelihood of inverse processes occurring when the electrons are slow and easily captured by the ionic species.

One side note regarding the differential cross section is that the output generated by the atomic code for ionization are integrated cross sectional values. In order to resolve this issue, the DCS profile used in this work is the hydrogen DCS equation which have been scaled to the cross sections produced by cFAC so that the original ICS is retained in the rate calculation. However, these DCS profiles can be replaced by more appropriate formulations should a complete set of profiles exist in the open.

C. Radiative Recombination

Complementary to the set of collisional events in a CR model are the radiation or photon-driven processes that can also alter the state of a plasma. While these rates were not explicitly derived by Le and Cambier, the

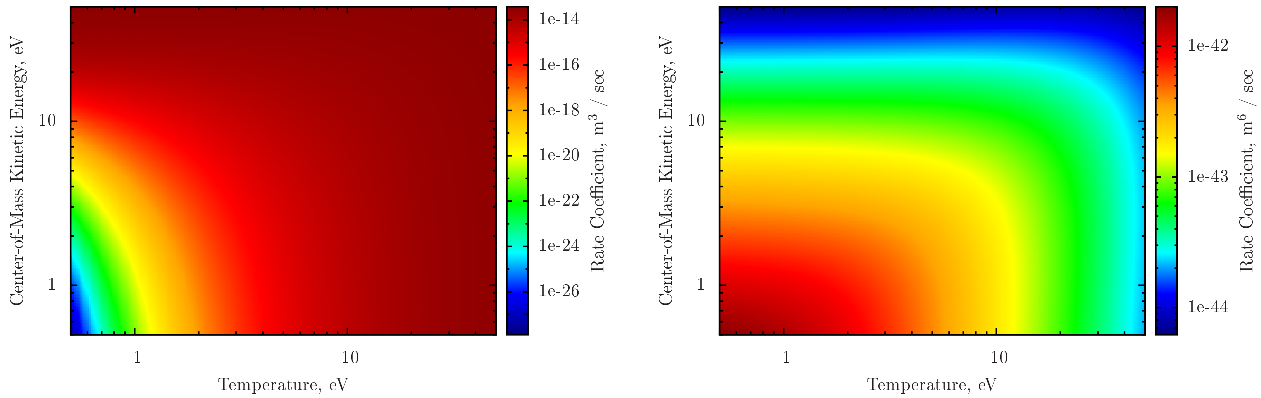

(a) Ionization (b) Recombination

Figure 3: Electron-impact ionization and three-body recombination multifluid rate coefficients between (lower state) Xe^{+1} $5p^3_{3/2}(J = 3/2)$ and (upper state) Xe^{+2} $5p^2_{3/2}(J = 2)$. The energy gap between both states as calculated by cFAC is 20.342 eV.

formulation for radiative recombination is a mere extension of the two-body multifluid rate derivations that were already performed. In this work, the optically-thin assumption has been imposed on the model so that no re/absorption takes place within the plasma whether by photoexcitation or photoionization. However, the multifluid modification clearly only extends to the radiative recombination rate equation because of its collisional nature. The rate of change in atomic state density due to radiative recombination is shown in Eq. 6 where the Milne relation has been applied to recast the equation in terms of the photoionization cross section.

$$\Gamma^{rr}_{su} = N_s N_u \overline{g}_{\tilde{T}} e^{-\lambda} e^{x^*} \left(\frac{k_B \tilde{T}}{m_e c^2} \right) \frac{g_l}{2 g_u} \int_{x=x^*}^{\infty} dx \; x^2 e^{-x} \overline{\sigma}^{pi}_{sl}(x) \zeta^{(0)} \left(\sqrt{\lambda (x - x^*)} \right) \tag{6}$$

Accounting for the energy equation's evolution due to radiative recombination is not as trivial when compared to the previous collisional processes' energy loss rates because discrete energy gaps are lost from the total electron energy. In the case of radiative recombination, a broadband loss in electron energy can occur since any excess energy beyond the ionization threshold is lost in the form of radiation during the recombination process. Therefore, an additional energy factor is multiplied within the radiative recombination energy coefficient's integrand to account for the energy loss of the system due to this particular process. This energy rate coefficient is shown in Eq. 7 below.

$$Q^{rr}_{su} = N_s N_u \overline{g}_{\tilde{T}} e^{-\lambda} e^{x^*} \left(\frac{(k_B \tilde{T})^2}{m_e c^2} \right) \frac{g_l}{2 g_u} \int_{x=x^*}^{\infty} dx \; x^3 e^{-x} \overline{\sigma}^{pi}_{sl}(x) \zeta^{(0)} \left(\sqrt{\lambda (x - x^*)} \right) \tag{7}$$

A sample set of radiative recombination density and energy rate coefficients are shown in Figs. 4a and 4b, respectively. The map of radiative recombination density rate coefficients shows a very similar contour map to the maps shown in electron-impact deexcitation and three-body recombination. But, the additional energy factor in the radiative recombination energy rate integration creates a different contour map which shows an increase in the rate coefficient as one traverses positively in COM kinetic energy. This is expected since an increase in COM kinetic energy simply means an increased energy loss in the form of radiation should the electrons with an additional streaming component recombine with the ionized species.

D. Elastic Collision

The last set of terms to be incorporated within the CR model are the elastic collision terms. These terms do not directly change the atomic state distribution, but do influence the overall set of reaction kinetics because of variations in temperature induced by elastic collisions. Both electron-neutral and electron-ion elastic collisions are being considered in this work. The form for higher-order moments of the inelastic

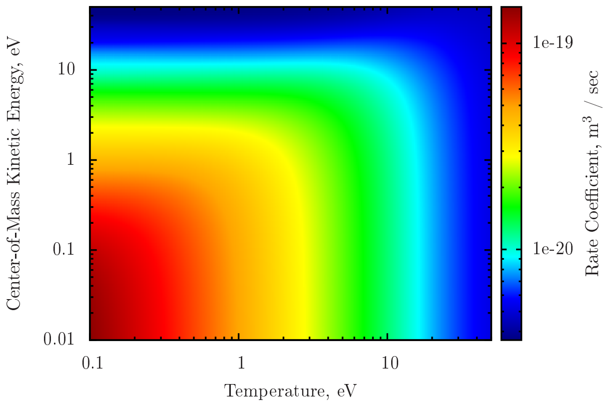

(a) Radiative Recombination

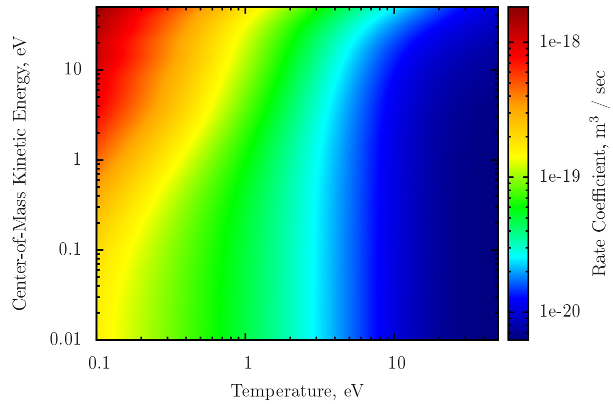

(b) Radiative Recombination Energy

Figure 4: Radiative recombination density and energy multifluid rate coefficients between (lower state) Xe^{+1} $5p^3_{3/2}(J = 3/2)$ and (upper state) Xe^{+2} $5p^2_{3/2}(J = 2)$. The energy gap between both states as calculated by cFAC is 20.342 eV.

collision processes which yield the momentum transfer and thermal relaxation rate coefficient equations, while accounting for the multifluid drift, was derived by Le and Cambier; although the paper solves the equation for a threshold energy gap, taking the energy gap to be 0 eV allows the equation to be solved for elastic collisions. The momentum transfer and thermal relaxation rates are shown below in Eqs. 8 and 9.

$$K^{en} = m_e N_e N^{+0} \frac{2}{3} \overline{g}_{\tilde{T}} e^{-\lambda} \int_{x=x^*}^{\infty} dx\ x^2 e^{-x} \overline{\sigma}^{en}(x) \left(1 - \langle \cos\chi \rangle_{\Omega'}\right) \zeta^{(1)} \left(\sqrt{\lambda x}\right) \tag{8}$$

$$J^{en} = N_e N^{+0} \overline{g}_{\tilde{T}} e^{-\lambda} \int_{x=x^*}^{\infty} dx\ x^2 e^{-x} \overline{\sigma}^{en}(x) \left(1 - \langle \cos\chi \rangle_{\Omega'}\right) \left[\zeta^{(0)} \left(\sqrt{\lambda x}\right) - \frac{2\lambda}{3} \zeta^{(1)} \left(\sqrt{\lambda x}\right)\right] \tag{9}$$

Integration of higher-order inelastic collision rate coefficients leads to the additional $\zeta^{(1)}$ factor elaborated below:

$$\zeta^{(1)} = \frac{3}{4\xi} \int_{-1}^{+1} dy e^{2\xi y} = \frac{3}{4\xi^2} \left[\cosh(2\xi) - \frac{\sinh(2\xi)}{2\xi}\right] \quad \text{s.t.} \quad \lim_{\xi \to 0} \zeta^{(1)} = 1 \tag{10}$$

Another aspect of the electron-neutral elastic collision rates is the $1 - \langle \cos\chi \rangle_{\Omega'}$ modifier, which when multiplied to the total elastic collision cross section yields the momentum transfer cross section. For electron-neutral Xe collisions, these cross sections were found in McEachran and Stauffer's elastic collision studies.[9] As before, rate coefficient maps were generated as a function of temperature and COM kinetic energy for the momentum transfer and thermal relaxation rate coefficients shown in Figs. 5a and 5b, respectively. A unique feature of these maps is the presence of multiple maxima as one traverses along the COM kinetic energy axis at low temperatures. This results from the Ramsauer-Townsend effect where the electron's wavelike interaction with each of the atom's electron shells results in a decreased collision cross section.[10,11]

Finally, the momentum transfer and thermal relaxation rate coefficients for the electron-ion elastic collisions can be determined by using Rutherford's scattering analytical DCS with a cut-off impact parameter based on the Debye length.[12] The integrated cross section is provided via Eq. 11:

$$\sigma^{ei,m} = \frac{e^4}{16\pi\varepsilon_0^2\epsilon^2} \ln\Lambda \tag{11}$$

Using the integrated cross section, closed form, analytical equations can be obtained for the electron-ion momentum transfer and thermal relaxation rate coefficients. These rate coefficients are still functions of both temperature and COM kinetic energy and are calculated through the course of the simulation instead of being tabulated like the previous collision rates.

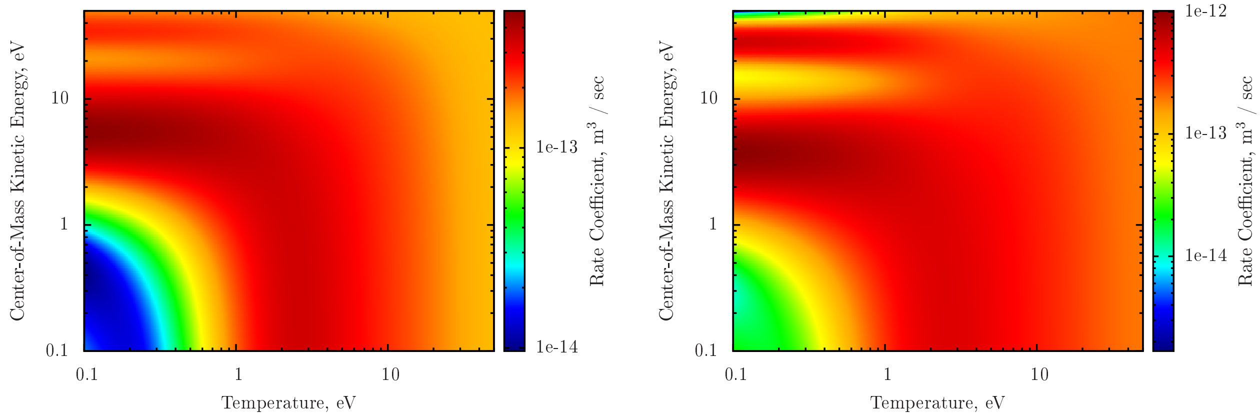

(a) Momentum Transfer (b) Thermal Relaxation

Figure 5: Elastic collision multifluid rate coefficients for Xe^{+0}. Subfigures 5a and 5bcorresponds to the momentum transfer and thermal relaxation rate coefficients, respectively.

$$K^{ei} = m_e N_e N^{+i} \frac{16\sqrt{\pi}}{3} \frac{q_i^2 e^2}{\mu^2 \alpha^3} \ln\Lambda \left[\frac{3\sqrt{\pi}}{4\lambda^{3/2}} \mathrm{erf}\left(\sqrt{\lambda}\right) - \frac{3}{2\lambda} \exp\left(-\lambda\right) \right] \tag{12}$$

$$J^{ei} = N_e N^{+i} 8\sqrt{\pi} \frac{q_i^2 e^2}{\mu^2 \alpha^3} \ln\Lambda \, \exp\left(-\lambda\right) \tag{13}$$

E. Steady-State Simulations

Steady-state Xe simulations were performed using the collisional-radiative model to determine the impact of the multifluid effect on the plasma. This was performed by observing the average charge of the xenon plasma as the electron temperature and center-of-mass kinetic energy are varied. By imposing a center-of-mass kinetic energy, one can imagine streaming electrons relative to stationary heavy species. For these steady-state simulations, the terms considered in the model include electron-impact excitation and deexcitation, electron-impact ionization and three-body recombination, along with the radiative processes of radiative recombination and spontaneous emission. All of the processes listed above, with the exception of spontaneous emission, use modified rates that account for the multifluid effect. The solution to this system was obtained by performing a linear solve of the atomic state distribution's master equations with no density rate-of-change and replacing one of the equations with the charge neutrality constraint. The results are shown in Fig. 6.

Figure 6 shows the average charge of the Xe heavy species as a function of temperature for 4 different center-of-mass kinetic energy differentials labeled as 'dKE' on the figure: 0 eV, 0.1 eV, 0.5 eV, and 0.75 eV. These simulations were conducted assuming an electron density of 1×10^{19} m^{-3}. The impact can be clearly observed as one increases the COM kinetic energy that the average charge correspondingly increases. For instance, a comparison of the 0.75 eV stream with the case of no bulk streaming shows that there is a 0.25 eV temperature difference for both cases to achieve the same heavy species charge. The difference is also readily visible for the 0.1 eV case as well. The streaming effect clearly impacts the steady-state kinetics and allows the excitation and ionization multifluid effect to produce higher average charge values in comparison to the non-streaming scenario.

III. Time-Dependent Evolution of Collisional-Radiative Equations

The last simulation performed in this work is a time-dependent investigation of the streaming electrons' effect on the evolution of the plasma. This simulation is intended to be a representation of the reaction kinetics during the formation of the plasmoid in a Field-Reversed-Configuration thruster. If one pictures an infinitesimal cell within the FRC channel where the weakly-ionized stationary Xe gas is bombarded by azimuthally-streaming electrons, this scenario would be captured by the temporal evolution of the CR model.

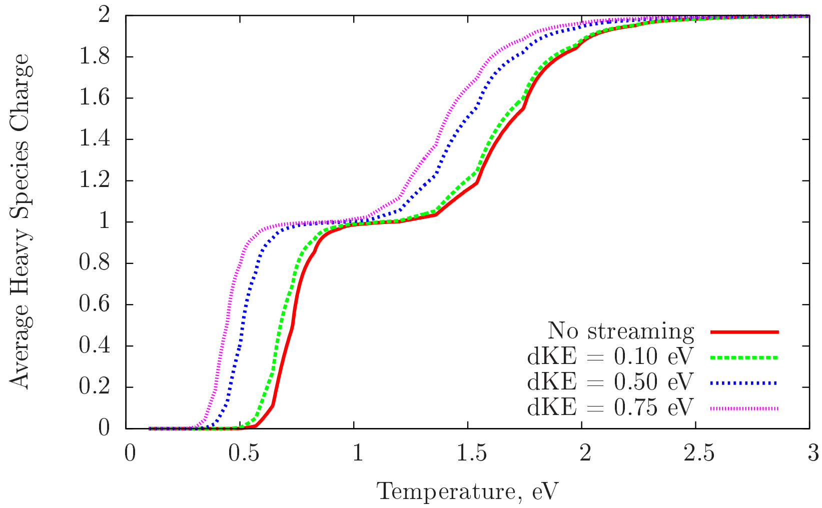

Figure 6: Steady State Ionization Fraction

The master equations corresponding to this model is described below.

A. Time-Dependent Master Equations

The time-dependent set of equations used to evolve the atomic state distribution function are shown below. The first equation shown in Eq. 14 represents the time rate of change of each atomic state density that is being modeled in the collisional-radiative model. The source on the RHS represents all of the collisional-radiative processes being considered for the atomic state's evolution. The additional equations, Eqs. 15 and 16 respectively, model the momentum and energy changes for both the electron and heavy species fluids.

$$\frac{dN_i^{+k}}{dt} = \Gamma_{+k,i}^{(inelas)} \qquad \text{for all ions, } +k\text{, and all respective states, } i \tag{14}$$

$$\frac{d(m_{\frac{e}{h}} N_{\frac{e}{h}} \mathbf{u}_{\frac{e}{h}})}{dt} = \mp \cancel{(\mathbf{u}_e - \mathbf{u}_h)\left(K^{(ec,neu)} + K^{(ec,ion)} + K^{(inelas)}\right)} \tag{15}$$

$$\begin{aligned} \frac{d\varepsilon_{\frac{e}{h}}}{dt} &= \mp \left(\overline{\mathbf{u}} - \mathbf{u}_{\frac{e}{h}}\right) \cdot (\mathbf{u}_e - \mathbf{u}_h) \left(K^{(ec,neu)} + K^{(ec,ion)} + \cancel{K^{(inelas)}}\right) \\ &\mp 2\frac{m_e}{m_h} k\,(T_e - T_h) \left(J^{(ec,neu)} + J^{(ec,ion)} + \cancel{J^{(inelas)}}\right) - \left[\Xi^{(inelas)}\right]_{(\mathrm{e}^-\ \mathrm{Eqn})} \end{aligned} \tag{16}$$

The momentum equations consists of the momentum transfer effects due to elastic electron-neutral and electron-ion elastic collisions, as well as inelastic collision processes which lead to changes in the ASD. In this study, however, these terms are being neglected in addition to the spatial considerations that come with solving the momentum equations. This was enforced so that the studies will be focused towards the formation of the plasma without the added complexity of a changing COM kinetic energy. Therefore, the streaming electron energy will be a constant throughout the course of the simulation, while the heavy species are assumed to be motionless in the bulk velocity.

Finally, the energy equations for both electron and heavy species are included, allowing for the evolution of the electron and heavy species temperatures. In this equation set, not only do the energy changes due to momentum transfer exist from the elastic collisions, but the variations caused by the thermal relaxation process from elastic collisions are also included. Since inelastic collisions also alter the energies of both fluids, there are corresponding momentum transfer and thermal relaxation rates due to these processes; the inclusion of these rates will be the subject of future CR studies. Lastly, the loss or gain of energy due to changes in the atomic state distribution, i.e. transition energy gap, must be incorporated in the electron equation.

B. Simulation Results

The simulation performed in this work is intended to capture the plasma generation process which takes place within a Field-Reversed-Configuration thruster. As such, the electron streaming energy has been fixed to 0.01 eV; this corresponds to prototypical parameters of electrons revolving at a frequency of 1 MHz around the thruster channel with a radius of approximately 6 cm. There certainly are no defined or standardized FRC thruster parameters as the thruster can be scaled for optimal performance parameters. The choice of dKE = 0.01 eV does not take a large advantage of the ionization rate as it approaches the thermal, non-streaming limit of the rate coefficients. But, slight increases in the thruster dimension or revolution frequency can more quickly lead to more variations in plasma characteristics. Using Backward Euler with Newtonian iterations to temporally evolve the system, the results generated from the simulation are shown in Figs. 7a to 8.

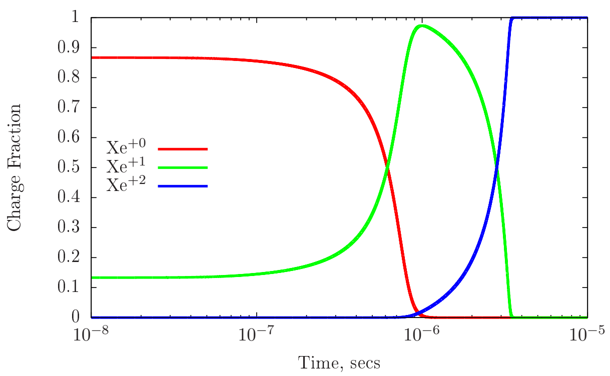

(a) Charge Fraction Evolution

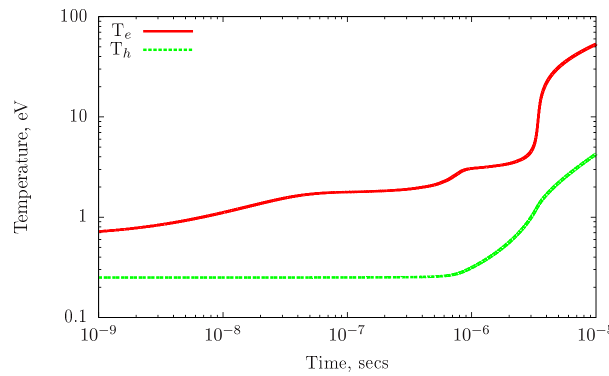

(b) Temperature Evolution

(c) Evolution of several parameters of the xenon plasma. To simulate the Field-Reversed-Configuration thruster's plasma generation, a constant electron streaming energy source has been assumed for the simulation.

Figure 7a shows the charge fraction evolution of each ionization stage of Xe considered in the model. From the simulation, an initial ionization fraction of 0.133 was assumed with a total heavy species density 1 $\times$ 10^{21} m^{-3}. The electron density was determined based on the quasineutral assumption. The results show that a majority of the neutral population has depleted at 1 μs, at which point the growth of Xe^{+2} begins as the Xe^{+1} population depletes. By the end of the simulation at 10 μs, most of the plasma consists of Xe^{+2} ions. The rapid rise in Xe^{+2} can be explained from the temperatures plot shown in Fig. 7b.

The initial electron temperature assumed for the simulation was 0.65 eV while the heavy species temperature was initialized at 0.25 eV. One can see that the constant streaming electron energy source leads to a continual rise in electron temperature. As each ionization stage peaks during the evolution of the plasma, sudden increases in electron temperature can be observed in the plot of the fluid temperatures. As the system continues to siphon energy from the constant electron energy stream, the electron temperature grows into the 10s of eV. The heavy species temperature eventually begins to equilibrate with the electron temperature at the μs timescale. It should be reiterated that these results are ideal with respect to the presence of a constant electron energy source, i.e. a true evolution of the electron momentum would have no constant electron energy source. A full simulation of the FRC formation would also require solving the fluids' momentum equations, accounting for the problem's spatial dimensionality, and incorporating other collisional terms which were not included in this simulation.

Figure 8 shows the rate of energy transfer due to the collisional processes involved in the simulation. The amount of energy provided by electrons led to larger electron energy losses due to electron-impact excitation and ionization as opposed to the gains provided the inverse processes. For the case of momentum transfer energy and thermal relaxation rates, the plot shows a larger energy exchange process through thermal relaxation in comparison to the momentum transfer rates. In the momentum transfer energy rate, it should also be noted that the energy increase due to the electrons' constant streaming energy is not factored into this term as shown in the plot. The last set of energy losses stem from the radiative processes which shows that spontaneous emission has the largest radiative sink term for most of the simulation's run.

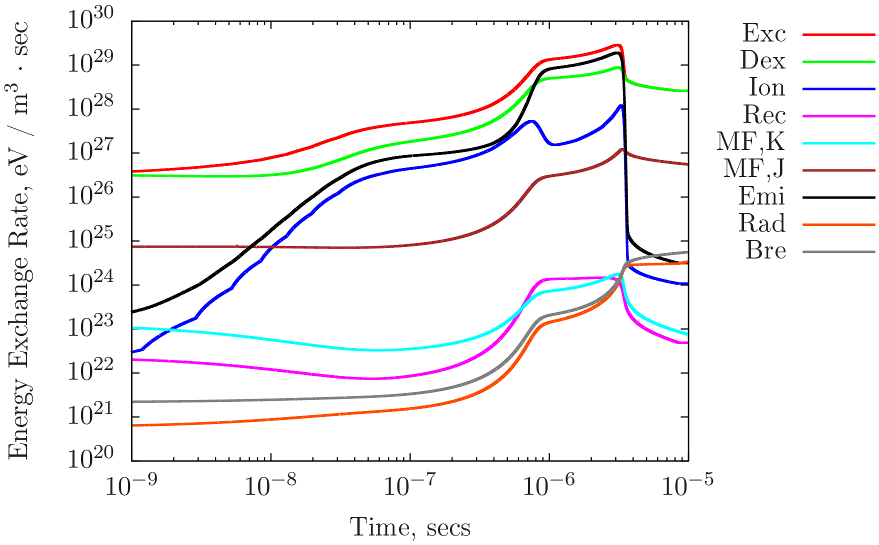

Figure 8: Evolution of the energy gain and loss rates due to multiple elastic and inelastic collision processes. The table lists energy variations caused by electron-impact excitation (Exc), deexcitation (Dex), ionization (Ion), three-body recombination (Rec), momentum transfer collisions (MF,K), thermal relaxation collisions (MF,J), spontaneous emissions (Emi), radiative recombination (Rad), and bremsstrahlung (Bre).

IV. Conclusion

The direction of future electric propulsion devices presents many challenges born out of these systems' increasing complexity as pursuits for better performance characteristics are sought. The Field-Reversed-Configuration thruster represents one such thruster at the forefront of propulsion research which has strong multifluid aspects that lead to the formation of the plasmoid. The multifluid reaction kinetics was presented as a contributing factor to the formation of the plasmoid, thereby leading to the implementation of multifluid rate coefficient calculations generalized for any atomic species. In this work, Xe^{+0} to Xe^{+2} were used to generate steady-state and time-dependent simulation results to determine the importance of multifluid effects in next generation of EP devices that may exhibit such characteristics.

In the steady-state simulations, average charge values of the Xe species were calculated for a range of electron temperatures and multiple center-of-mass kinetic energy values. It was shown that for values as small as tenths and even hundredths of eV, the difference in average charge states can be observed in the system. On the other hand, the objective of the time-dependent simulation is to show the contribution of the relative multifluid streaming effect through several plasma parameters. Although the transience of the simulation does not capture the effects as immediately as the steady-state simulation, the impact of the streaming electrons as an energy source term is visible in the growth of the ionizing plasma.

These simulations helped elucidate the importance of multifluid reaction kinetics within the FRC thruster. But, a more thorough simulation incorporating additional energy terms and spatial/fluid effects are needed to capture the FRC thruster's plasmoid formation and ejection physics. Multifluid reaction rate kinetics may also be significant for more exotic electric propulsion concepts and other physical devices beyond the electric propulsion community. As such, much work involving these multifluid effects and their impact on many plasma physics devices will continue to be pursued in the future.

Acknowledgments

The authors would like to thank Hai P. Le (LLNL) for stimulating discussions.

This research was performed while R. J. E. Abrantes held an NRC Research Associateship award at the Air Force Research Laboratory (AFRL, Edwards AFB) under grant No. FA9550-18-D-0002.

The authors would also like to acknowledge support provided by the Air Force Office of Scientific Research

(AFOSR) grant No. FA9550-17RQCOR465 (PO: Dr. Mitat Birkan).

References

[1]Hugrass, W., and Grimm, R. *A numerical study of the generation of an azimuthal current in a plasma cylinder using a transverse rotating magnetic field*, Journal of Plasma Physics, 26(3), 455-464, 1981.

[2]Slough, J., Kirtley, D., and Weber, T. *Pulsed plasmoid propulsion: The ELF thruster*, 31th International Electric Propulsion Conference, 20-24, 2009.

[3]Boeuf, J.-P. *Tutorial: Physics and modeling of Hall thrusters*, Journal of Applied Physics, 121, 011101, 2017.

[4]Sousa, É. M. *A Blended Finite Element Method for Multi-Fluid Plasma Modeling*, Ph.D. thesis. University of Washington, 2014.

[5]Le, H. P., and Cambier, J. L. *Modeling of inelastic collisions in a multifluid plasma: Excitation and deexcitation*, Physics of Plasmas, 22(9), 093512, 2015.

[6]Le, H. P., and Cambier, J. L. *Modeling of inelastic collisions in a multifluid plasma: Ionization and recombination*, Physics of Plasmas, 23(6), 063505, 2016.

[7]Stambulchik, E. *cFAC*, https://github.com/fnevgeny/cfac.

[8]Kramida, A., Ralchenko, Y., Reader, J., and NIST ASD Team (2018). *NIST Atomic Spectra Database* (ver. 5.6.1), [Online]. Available: https://physics.nist.gov/asd [2019, August 5]. National Institute of Standards and Technology, Gaithersburg, MD.

[9]McEachran, R. P., and Stauffer, A. D. *Momentum transfer cross sections for the heavy noble gases*, The European Physical Journal D, 68(6), 153, 2014.

[10]Ramsauer, C. *Über den Wirkungsquerschnitt der Gasmoleküle gegenüber langsamen Elektronen*, Annalen der Physik, 6(64), 513-540, 1921.

[11]Townsend, J. S., and Bailey, V. A., *XCVII. The motion of electrons in gases*, The London, Edinburgh, and Dublin Philosophical Magazine and Journal of Science, 42(252), 873-891, 1921.

[12]Burgers, J. M., *Flow equations for composite gases*, Maryland Univ College Park Inst for Fluid Dynamics and Applied Mathematics, 1969.